Materials and Design 187 (2020) 108360

Contents lists available at ScienceDirect

Materials and Design

journal homepage: www.elsevier.com/locate/matdes

Ductile deformation in alumina ceramics under quasi-static to dynamic contact impact

Robert G. Crookes, Benjamin März, Houzheng Wu *

Department of Materials, Loughborough University, Leicestershire LE11 3TU, UK

HIGHLIGHTS

- Dislocation gliding under all impacts is governed by the Hertzian shear stress field with a critical level of 2.54 ± 0.10 GPa for armour alumina.
- Higher shear stress leads to higher dislocation densities up to 10^{16} m^{-2}. The maximum is measured in a plastic flow band under ballistic impact.
- The ductile deformation observed under all contact impacts is independent to fracture patterns and degree of fragmentation.

GRAPHICAL ABSTRACT

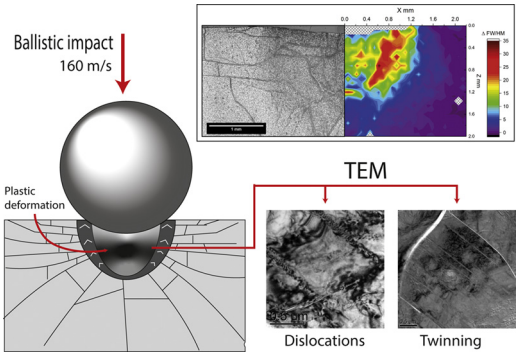

ARTICLE INFO

Article history:
Received 30 July 2019
Received in revised form 12 November 2019
Accepted 13 November 2019
Available online 16 November 2019

Keywords:
Plastic deformation
Alumina
Dislocations
Impact
Armour
Indentation

ABSTRACT

Cr^{3+} Fluorescence spectroscopy and TEM have been used to study the ductile deformation of alumina ceramics underneath an impact contact. The contact was generated by a spherical tungsten carbide indenter under quasi-static, drop weight and ballistic loading conditions. In all circumstances, a ductile deformation region containing dislocations developed below each contact impression. The dislocation density distribution complies with the shear stress distribution predicted by the Hertzian contact model. Ballistic loading resulted in secondary material flow, giving a maximum dislocation density 5–10 times higher than that dictated by the Hertzian contact model. Quantification of dislocation density distribution allowed a critical shear stress for dislocation generation to be estimated. In this alumina ceramic, the critical shear stress is estimated at 2.55 ± 0.10 GPa. Cold work hardening and comminution under dynamic loading are discussed as possible mechanisms for the enhanced dislocation activity under dynamic impact.

1. Introduction

Ceramic materials have been used in armour systems since the Vietnam war, where alumina backed by fibreglass composite was applied as lightweight armour to aircraft [1]. This example highlights the two main advantages of using ceramics in armour systems. Ceramics are light weight and hard, making them capable of defeating steel armour penetrating rounds whilst offering significant weight savings when compared to an equivalent performing steel armour.

Shockey et al. identified some key material properties and engineering attributes governing penetration resistance of confined ceramic tiles [2]. Physical properties such as hardness and compressive strength are required to be high in order to deform or fracture a projectile at early

* Corresponding author.
E-mail address: h.wu2@lboro.ac.uk (H. Wu).

https://doi.org/10.1016/j.matdes.2019.108360

stages of contact. Engineering attributes such as the pulverization characteristics, frictional flow characteristics of fine fragments, and fragment abrasiveness likely govern the penetration resistance of the ceramic. Later, these findings were supported by Krell and Strassburger who determined the order of influences of different mechanical properties and failure modes of alumina on its ballistic resistance [3]. It was concluded that projectile erosion through ceramic debris abrasion, and projectile dwell at early stages of impact, are the primary and secondary mechanisms, respectively. By now, many researchers have attempted to develop possible screening tests for differentiating ballistic resistance among ceramics, and quasi-static hardness tests are most commonly performed because hardness is recognised as a major index of potential ballistic performance through governing the dwell time [4,5].

Nonetheless, the rational for using hardness as a ballistic performance index for a ceramic armour design is not widely accepted due to conflicting evidences. The hardness measurement of a ceramic is determined through indentation size, which is produced through the combined effect of cracking and ductile deformation through lattice slip [6]. Hallam et al. proposed a multi approach technique using Knoop and Vickers hardness tests coupled with the induced fracture form to predict ballistic performance [7]. Using a detailed layer by layer polishing technique the crack formation under indents was 3D mapped. The different crack formations were then correlated with variations in ballistic performance not accounted for by hardness alone. One fundamental assumption here is that the crack formation induced in a quasi-static test is comparable to that of a dynamic impact. This is partially supported by Anderson et al., who determined that under quasi-static and dynamic indentations no significant difference in radial crack frequency and length can be observed for indentations with equivalent indent diameters [8].

All these studies tend to focus on brittle fracture under dynamic loading conditions. Most recently, however, Wu et al. conducted a thorough analysis of recovered fragments of armour alumina ceramics after ballistic testing [9]. It was found that ductile deformation with high dislocation activities had a strong link with fragment sizes. Smaller fragments tend to have more dislocations, and when a fragment is larger than a critical value of about 1200 μm, there are no detectable dislocations. It is this research that leads one to believe that the understanding of dynamic damage of ceramic needs to have both brittle fracture and ductile deformation considered together.

In addition, the plastic deformation identified with fluorescence spectroscopy is verified using TEM, where a significant quantity of dislocations and lattice slip is observed.

1.1. Plastic deformation in ceramics

Ductile deformation in the form of dislocation generation and glide is well documented and has been observed both at quasi-static and dynamic strain rates. The onset of plastic deformation requires stress greater than that of the bulk tensile, bending, or compressive strength of the material. Instead high confinement is required.

By the early 1960s it had been established that ductile deformation in metals was caused by the generation and migration of dislocations in the atomic lattice. At this time, it was widely agreed that such dislocations could not produce plastic deformation in ceramics at room temperature because of the strength of the covalent bonds. Many high temperature indentation hardness tests were performed [10–14], typically between 750 and 1900 °C, and it was determined that many ceramics including alumina had a brittle-ductile transition temperature where plastic deformation can occur. Hockey was the first to observe the formation of dislocations in alumina at room temperature [15]. The dislocations and associated plastic deformation being induced using a sharp indenter. Later work determined that, in alumina, plastic deformation most commonly occurs through basal and prismatic slip, mostly in basal twins and dislocations [16–18].

Lawn et al. performed high load spherical (Hertzian) indentations on numerous ceramics including alumina [19] [20] [21–23]. It was determined that there was a grain size effect on the generation of dislocations over microcracking. A grain size threshold of approximately 20 μm was observed, below which plastic deformation was dominated by twin and dislocation generation [22].

Wu et al. conducted further investigations on how secondary nanoparticles changed the ductile deformation of alumina ceramics [24,25], and their research has evidenced that dislocation activities in ceramics can be interfered with by hard dispersants and grain size, and relatively easy twins along basal plane can be restrained by nanoparticles.

Above, all plastic deformation was generated either through quasi-static indentations or through surface abrasion. Longy and Cagnoux noted that in addition to fragmentation, dislocations/twins were formed during high-velocity impacts [26]. Many dynamic high energy tests have been used to induce plastic deformation in alumina, including split Hopkinson pressure bar (SHPB) [27,28], flyer plate, explosive compression [29], laser peening [30], and gas gun [31,32].

The work of Dancer et al. is of particular relevance as it combined several experimental methods which will be applied in this work, namely quasi-ballistic testing with optical microscopy and Cr^{3+} fluorescence spectroscopy [31]. These techniques were combined to both assess the fracture patterns and quantify residual stress and plastic deformation of dynamic indentations in alumina. 3 mm diameter pointed rods of 0.46 g were accelerated to 100 m s^{-1} (2.3 J impact energy), impacting the polished surface of polycrystalline alumina. The resultant residual stress and plastic deformation was consistent with the Hertzian contact models, fracture and residual stress conforming to a blunt contact stress field and the plastic deformation agreed with a sharp indenter blister field. Whilst these contact models are slightly contradictory it was reasoned that the plastic deformation occurred under the sharp tip of the projectile, which was then blunted at a later stage of impact to produce large scale stress fields consistent with a blunt contact.

Wade et al. identified several mechanisms of deformation in alumina under both quasi-static and dynamic indentation. Three stages of indentations were observed for both quasi-static and dynamic indents [33].

1. **Initial loading**: Shear-induced deformation in the form of dislocation pileups and twins generates stress along grain boundaries.
2. **Micro-crack initiation**: When the stress reaches a critical level, such that it surpasses the strength of the grain boundary, micro-cracking takes place.
3. **Pseudo-ductile behaviour**: As well as the initial plasticity, subsequent deformation is facilitated by grain boundary sliding, leading to the generation of a residual crater.

Here “plastic deformation” is defined as deformation purely occurring due to the formation and motion of dislocations. The total contribution of dislocations, microcracking and grain boundary slip is referred to as ductile deformation. In the literature this distinction is often not made, with any permanent indentation being classified as plastic deformation. In this work, Cr^{3+} fluorescence spectroscopy was used to quantify dislocation densities within ductile deformation in alumina. Therefore, reference to plastic deformation in this work is in regards to the content of dislocations.

Fragmentation, flow and abrasion occur under high energy impacts where the penetration threshold of the ceramic is exceeded. This makes small scale testing challenging. In addition, full scale testing often leaves very little usable material that can undergo characterisation. In this work the early stage impact damage is characterised using low velocity ballistic testing. In the following work any commonality between quasi-static Hertzian indentations, small scale drop weight impact tests, and ballistic impacts are explored; focusing on damage mechanisms along with the form and prevalence of plastic deformation.

It is the objective of the study to develop an increased understanding of plastic deformation in alumina ceramics and its relevance to high strain rate indentation such as that experienced during a ballistic impact. Any similarities between quasi-static and high strain rate deformation may provide scope for quasi-static screening tests when assessing ceramic armour performance. Furthermore, the quantification of plastic deformation, and determination of critical property values such as yield stress, is highly beneficial in the development of future models for predicting ceramic armour performance.

2. Experimentation

2.1. Indentations

All indentations were performed on the same grade and batch of alumina tiles. Indentations across all loading rates were performed with the use of the same tungsten carbide spheres with a diameter of 5 mm. This allowed direct comparisons to be made between different loading rate indentations. Ball indenters/projectiles were used in an attempt to produce consistent and repeatable indentations that are representative of early stage impact, where it has been shown that projectile blunting occurs during dwell. A minimum of three indentations were performed for each experimental parameter.

2.1.1. Quasi-static

Quasi-static (QS) spherical Hertzian indentations were performed on a compression/tension tester (Lloyd Instruments LR50K plus, UK). Loads were applied at a speed of 0.01 mm s^{-1} to reach different levels of load, 10, 14, 18 and 22 kN before unloading for conducting post-indentation examination of the indents. When indentations were performed at multiple positions on the same surface, the minimum space between two indents was set as 10 mm.

2.1.2. Dynamic

Small scale drop weight (DW) impact testing, similar to that used by Wade et al. [6], was performed on the alumina tiles. The alumina tile was placed on a 10 mm thick steel plate and held in place by a thin layer of vacuum grease. This was to remove air gaps between the tile and plate to aid the transmission of stress waves. Drop weight impacts were performed with two weights, 0.63 kg and 1.38 kg from a height of 0.50 m in air at room temperature, resulting in an estimated impact velocity of 3.15 ms^{-1} and giving impact energies of 3.07 J and 6.76 J respectively.

2.1.3. Ballistic

Quasi ballistic impacts were performed using a single stage light gas gun (Sabre Ballistics, Surry, UK) with a 7.62 mm calibre barrel. Tungsten carbide balls were used with a nylon sabot to provide a good fit to the barrel. Nitrogen gas at 50 bar was used to accelerate the WC ball to a velocity of 160 ± 10 m s^{-1}.

Much like drop weight tests, alumina tiles were mounted on a 10 mm thick mild steel plate with a thin layer of vacuum grease between the steel and alumina in order to remove air gaps that could hinder the transmission of stress waves to the steel backing plate. Here a single impact was performed on each tile, with a total of four tiles being tested.

2.2. Materials

All experimentation was performed on Sintox™ CL alumina 98.6% (Morgan Advanced Materials) in squared tiles with an edge length of 50 mm and thickness of 15 mm. All testing faces of the tiles were ground and polished (Kemet lapper/polisher, UK) with a finish by diamond suspension of 1 μm grit size. In all tests, tungsten carbide indenter balls were used. The typical materials properties are summarized in Table 1 for the alumina and tungsten carbide, as provided by the suppliers.

2.3. Characterisation

The resulting permanent indentations from both QS and DW tests were measured using white light interferometry (Zygo Newview 5000, USA). Surface topography maps were generated with a lateral resolution of 1.18 μm and vertical resolution of 3 nm. Permanent indents from ballistic impacts were measured using confocal microscopy (Alicona InfiniteFocus, Austria) with a 10× objective lens, which allowed the generation of surface topography maps to be compared to those of QS and DW indents.

Cross-sections were taken through selected indents. In the case of ballistic indents, where tile failure occurred, the tiles were mounted in epoxy with vacuum assisted degassing, prior to sectioning. This was to preserve, as best as possible, the comminuted and highly fractured zones within the indent. All sections were mounted, followed by grinding and polishing to have a surface finish by diamond suspension of 1 μm grit size on a semi-automatic polisher (Struers LaboForce, Germany). The as-polished cross-sections were examined using optical microscopy (Leica DMi8 Inverted Microscope, Germany). Large area images were generated through the automated stitching of microscopy images using the microscope's controlled stage.

2.3.1. Quantifying plastic deformation

Cr^{3+} Al_2O_3 fluorescence spectroscopy was used for quantifying dislocation density in alumina. The dislocation density being determined by the breadth (FWHM) of the Cr^{3+} primary peak at 14,400 cm^{-1}. The technique is described by Wu et al. [34] and has previously been applied to the measuring of indent damage zones and residual stresses by Dancer et al. [31] and Wade et al. [6].

Cr^{3+} fluorescence spectroscopy line scans and mapping were performed using a true confocal Raman microscope (Horiba, Japan) over a spectrum of 14,250–14,550 cm^{-1} with a 633 nm red line He-Ne laser. A 50× objective lens with a numerical aperture of 0.55 was used, giving a spot size of ≈1.4 μm when the laser is projected on the surface. A confocal setup was used to ensure the probing position is confined on the surface. Subsurface contribution to the fluorescence depends on the probe size, which is unknown in this testing. When large line scans and maps were performed, auto focus was applied. Each spectrum was captured twice for a duration of 1 s each, resulting in a total capture time of 2 s.

Maps and line scans were performed on cross-sections through selected indents. A scanning step of 10 and 50 μm were used for line scans and maps respectively. Reference spectra were taken from the associated polished surface at a distance from the damage zone sufficiently distanced to have not been affected. Acquiring reference spectra on a polished surface negates any measurement of dislocations induced by the polishing process.

Table 1
Mechanical property data for tungsten carbide balls and alumina tiles.

Material	Density (g/cm^3)	Young's Modulus (GPa)	Grain size (um)	Compressive strength (GPa)
Sintox™ CL (98.6% alumina)	3.89	380	4.0	2.0
Cobalt Binder Tungsten Carbide - K20	14.42	650	1.2–1.6	4.6–5.8

Values of dislocation density were calculated from the measured ΔFWHM. A full explanation of the calculation is presented by Wu et al. [34]. Here is presented a simplification of the full works.

$$\sqrt{(\Delta\mu^2)} = KF(\rho) \tag{1}$$

where

$$K = \frac{Gb}{2\sqrt{2\pi(1-\nu)}}\left\{(5+12\nu+2\nu^2)\Pi_a^2 + 2(1-2\nu)\Pi_a\Pi_c + \Pi_c^2\right\}^{\frac{1}{2}} \tag{2}$$

and

$$F(\rho) = \sqrt{\rho ln(1/b\sqrt{\rho\pi})} \tag{3}$$

For alumina the values of the required physical constants are: G = 150 GPa, $\nu = 0.24$, $b = 0.476$ nm for the $1/3(2\bar{1}\bar{1}0)$>Burgers vector, $\Pi_a = 2.7$ cm^{-1}/GPa and $\Pi_c = 2.15$ cm^{-1}/GPa [35]. Using these values and Eqs. (1) to (3), the predicted broadening can be calculated as a function of dislocation density.

Plastic deformation in ballistic indents was further characterised using TEM. Regions in indent sections selected for TEM imaging have high dislocation density predicted by Cr^{3+} fluorescence spectroscopy. Focused ion beam microscopy (FIB) was applied to prepare electron transparent thin foil specimens using a FEI Nova 600 Nanolab™ DualBeam™ system (Thermo Fisher Scientific, Oregon, USA). To protect the desired sample surface, a platinum (Pt) strip was deposited using the ion beam prior to the sample milling. Specimens were extracted from the sample *in-situ* using an Omniprobe™ micromanipulator, glued to a copper half-grid and finally thinned to electron transparency.

The specimens were examined using a FEI Tecnai F20 (Thermo Fisher Scientific, Oregon, USA) transmission electron microscope, operated at 200 keV.

3. Results

3.1. Indentation size and appearance

Fig. 1 shows optical microscopy, stereo microscopy, and macro photography of QS, DW and ballistic impact indentations on the polished alumina surface. It can be observed here that all dynamic and ballistic indentations exhibit some form of concentrated central damage inside plastically deformed indents. DW indents showed non-concentric arching cracks outside of the indenter contact zone. These arching cracks are not observed in QS indents. They are also not observed on ballistic indents; however, darkening around the ballistic indents from the projectile prevents clear observation of this area. Non-concentric arching cracks can be observed within the ballistic indent.

QS, DW and ballistic indents all present a clear permanently deformed indentation with a well-defined radius, as shown in Fig. 2. In QS and DW indents a central "plug" feature can be observed within the permanent indent. This feature is likely to be related to the early formation of ring and subsequent cone cracks. This "plug" feature is not observed in the ballistic indents, but it is likely that it has been consumed by the comminution zone. There is visual evidence of this central damage region in Fig. 1d and e.

White light interferometry and confocal microscopy allowed the quantification of indent size and geometry. Fig. 2 shows a representative

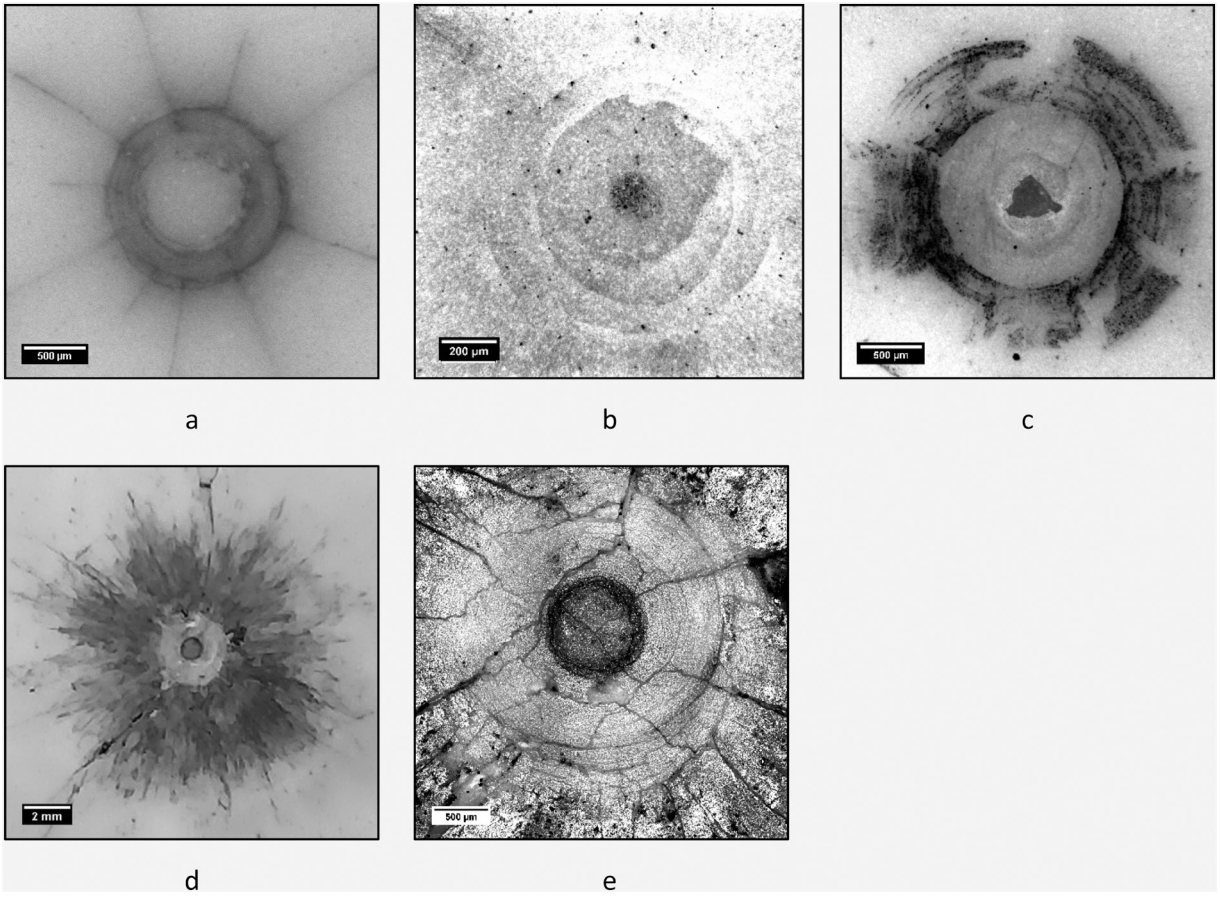

Fig. 1. Stereo, macro, and confocal imaging of indentations. (a)22 kN QS, (b) 0.68 kg DW, (c) 1.83 kg DW, (d) macro photography of ballistic indent, (e) confocal microscopy image of ballistic indent.

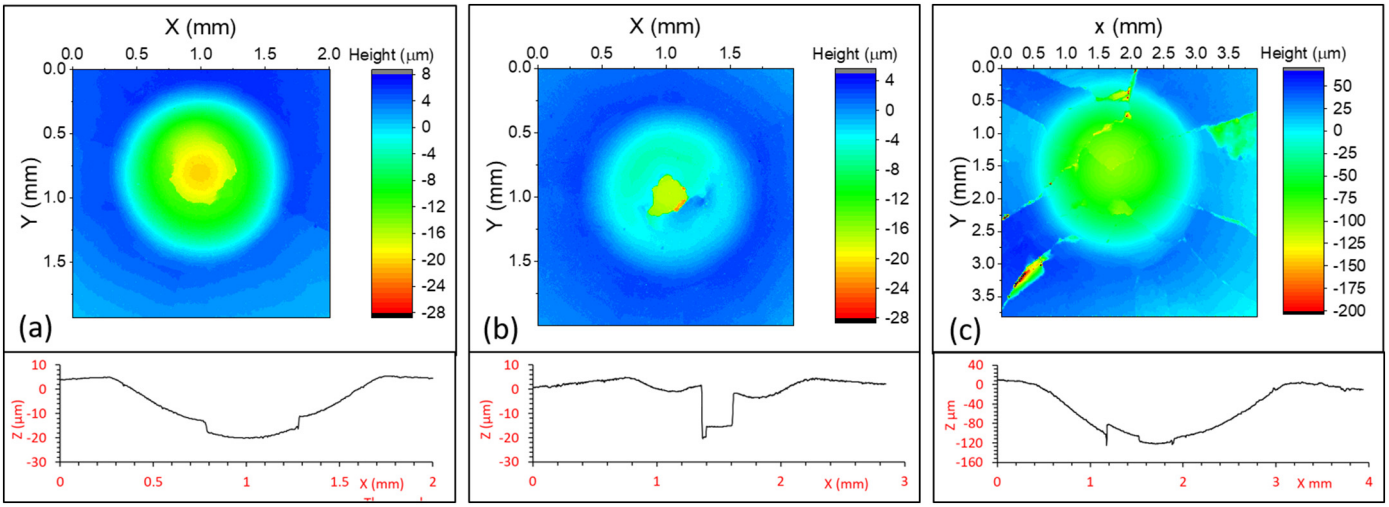

Fig. 2. Surface topography maps and centered section profile plots of (a) 22 kN quasi-static, (b) 1.38 kg dropweight and (c) ballistic indents.

QS, DW, and ballistic indent. All indents have a well-defined radius which takes the form of a raised lip around the indent. The depth of the indent is not as well defined. There is a large variability in depth, particularly with DW and ballistic indents, as fractured material is ejected. This often led to a central "plug" feature, observed as the dark regions in Fig. 1.

Table 2 presents indent diameters. It is clear here that the ballistic impact resulted in a significantly larger indent, consistent with the increased energy of the impact over that of the DW tests. Using the known QS loads to indent diameters, equivalent loadings were estimated for DW impacts. 0.63 and 1.38 kg drop masses were estimated to have 10 and 20 kN impact loads respectively. For QS indents, a mean indentation pressure was calculated based on the known indent load and diameter of the residual indentation.

3.2. Cross-sections

Large area optical microscopy of sections through indents revealed crack morphology that differed significantly between indentation rates, as shown in Fig. 3. QS indents showed a crack morphology consistent with Hertzian type overloading, with multiple shallow cone cracks propagating from surface ring cracking. Radial and median cracking was also clearly observed. There was little evidence of lateral cracking.

DW indents produced a crack morphology distinctly different to that of the QS. Most noticeably, the DW indents exhibited a large cone crack which appeared to have originated in the center of the indent either at the surface or sub-surface. The fragmentation and displacement of this cone produced the central plug feature observed previously. Another striking difference between the QS and DW indents is the extensive lateral cracking present in DW sections. Lateral cracking is commonly associated with the unloading of the indenter. It is reasonable therefore to assume that the extensive lateral cracking in DW indents is due to the rapid unloading of the indenter, cracking occurring where plastic deformation prevents elastic recovery.

Spall type cracking is observed in DW indents. These cracks appear to initiate at the primary cone and propagate laterally until they reach the surface of the tile. These spall cracks are likely responsible for the non-concentric arching cracks observed on the surface of the tiles.

Both QS and DW sections show a darker region of polishing induced pull-out directly under the indents. This region of fragile material is indicative of a comminuted zone, or the precursor to one.

When DW indents are compared to the ballistic indents there is a significant increase in the fragmentation of the alumina, consistent with the increased kinetic energy of the projectile. The central region of the ballistic indent showed an extensive comminuted zone extending to a depth of approximately 1.2 mm. The region surrounding the comminuted zone was highly fragmented, consisting of a combination of radial, lateral and cone type cracking.

There is some minor spall cracking identified in the ballistic indent. The change in spall cracking, when compared to DW, may be related to the stage of indentation at which the release waves occur. In dropweight indents the spall cracks are clearly linked to the primary cone crack from which they may initiate. This cone crack is not as well defined in the ballistic indent and occurs at a greater depth. The extent of cracking within the ballistic indent is likely to hinder the propagation of large-scale spall cracks.

Ballistic indents showed little evidence of a cone fracture, median (vent) cracking being the predominate fracture form directly under the impact. This may be due to the classic Hertzian contact stress field being overridden by a new stress field.

Table 2
Diameters and loads/energies for QS, DW, and ballistic indentations.

Test type	Load kN	Impact Energy j	Indent diameter mm (2r)	Mean indent pressure GPa
Quasi-static	10	–	1.02 ± 0.01	12.19
	14		1.20 ± 0.03	12.26
	18		1.35 ± 0.01	12.58
	22		1.49 ± 0.02	12.68
Drop weight	10[a] (0.63 kg @ 3.15 ms^{-1})	3.07	1.04 ± 0.02	–
	20[a] (1.38 kg @ 3.15 ms^{-1})	6.76	1.42 ± 0.05	–
Ballistic	1.0 g @ 160 ms^{-1}	12.8	3.04 ± 0.25	–

[a] Values estimated from quasi-static indent diameters.

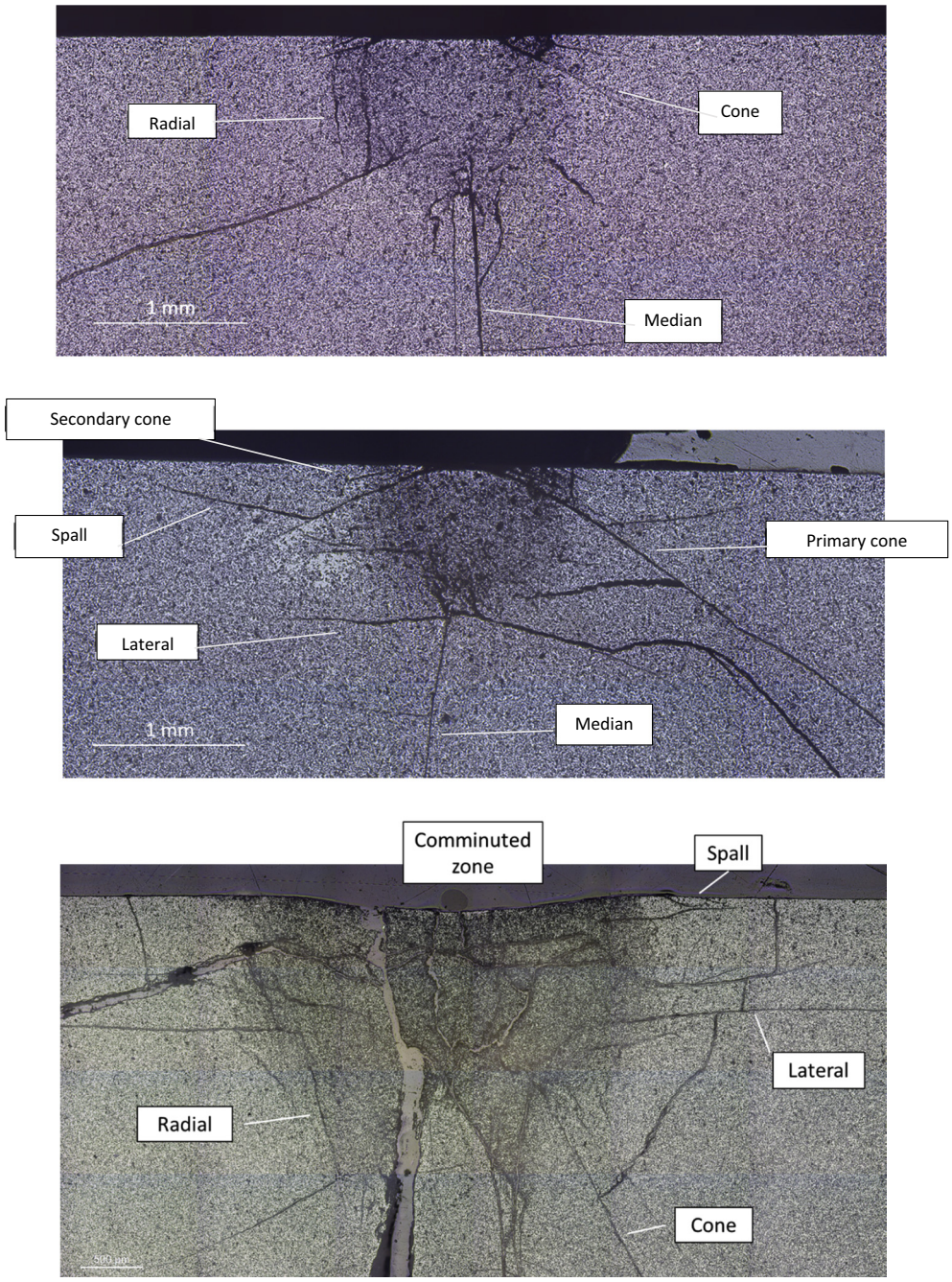

Fig. 3. Large area optical microscopy of sections through indents. (Top) Quasi-static, (Mid) Drop weight, (Bottom) Ballistic.

3.3. Plastic deformation

Cr^{3+} fluorescence spectroscopy maps of indent sections showed high values of dislocation density associated with all indentations, indicating extensive plastic deformation, as shown in Fig. 4. QS and DW indentations had a similar distribution of plastic deformation. The maximum ΔFWHM being 14 cm^{-1} and 10 for QS and DW respectively, corresponds to a dislocation density of 2.2×10^{15} and 1.0×10^{15} m^{-2} respectively. The maximum ΔFWHM occurred at a depth of ≈0.5*a*, where *a* is the indent radius. This distribution of dislocation density is consistent with the Hertzian ball contact shear stress field.

Mapping of the ballistic indent section initially revealed a dislocation density distribution different to that observed in QS and DW indents. Fig. 4c shows high ΔFWHM (>20 cm^{-1}) bands at the periphery of the dislocation region. These bands are broad near the surface, becoming thinner until they meet under the indent centre at a depth of ≈1.2 mm (0.8 the indent radius), forming a hemispherical shape. Values of ΔFWHM in this region vary from 20 to 35 cm^{-1} with corresponding dislocation density values of 5×10^{15} to 2×10^{16} m^{-2}.

3.3.1. Section line scans

Cr^{3+} fluorescence spectroscopy line scans of sections through indents were performed in the centre of the indent and extended down along the indentation loading axis to a depth of twice the permanent indent radius. DW and QS line scans showed similar Δ FWHM distributions, with the QS indent showing slightly increased values, as shown in Fig. 5. This is consistent with the indent's larger diameter. Both QS and DW indents showed a maximum Δ FWHM at a depth of 0.4–0.7 Z

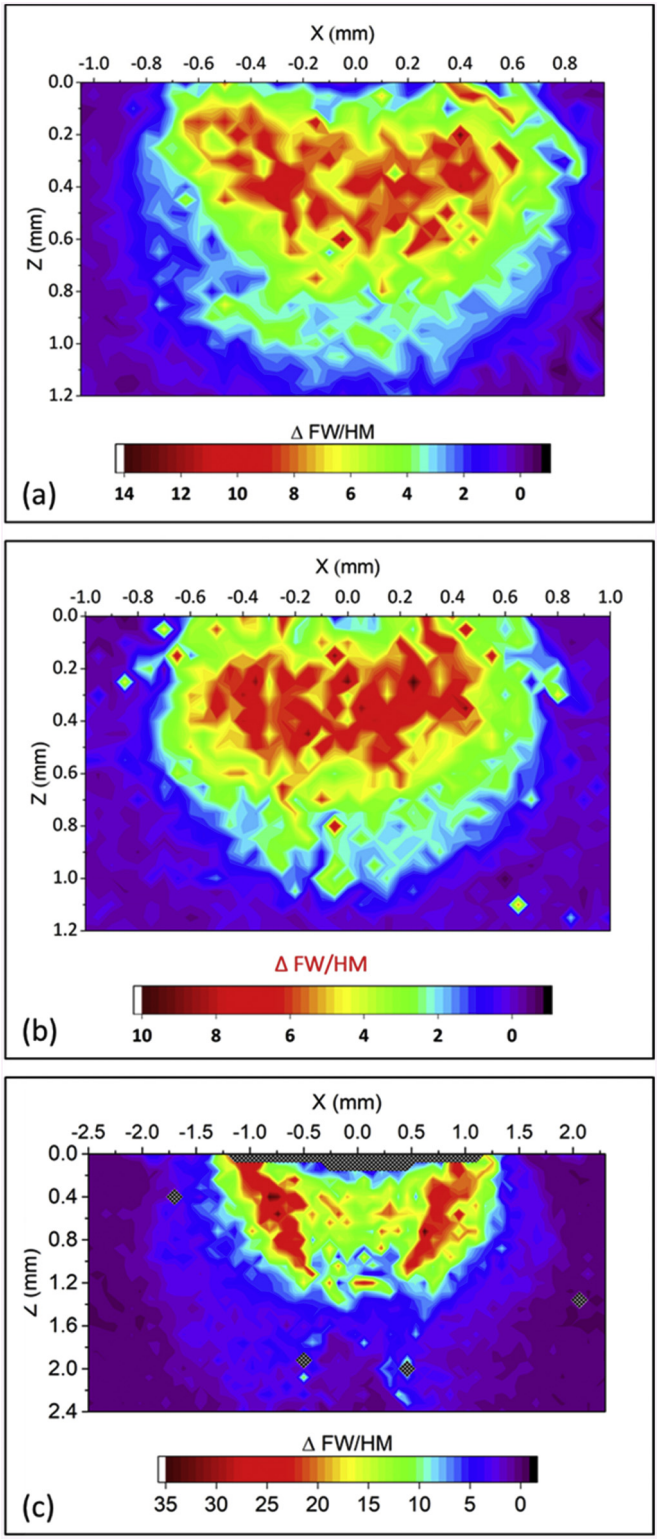

Fig. 4. ΔFWHM Cr^{3+} fluorescence maps of sections through indents. (a) Quasi-static, (b) drop weight, (c) ballistic.

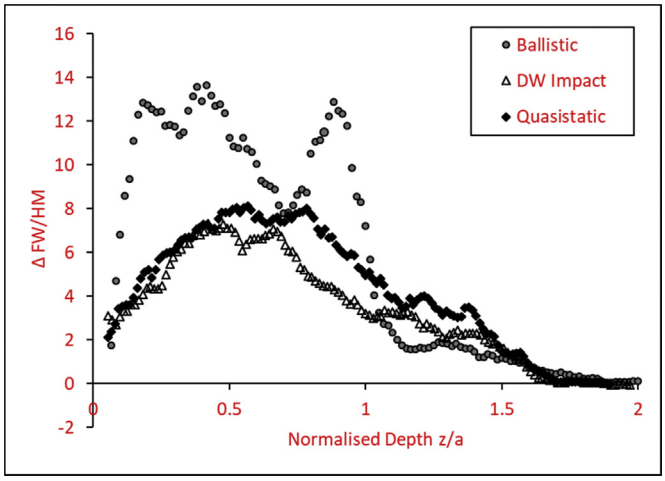

Fig. 5. Line scans from sections through indents. Scans originate in the center of the indent and extend perpendicular to the surface along the axis of indentation. Fluorescence spectra broadening (Δ FWHM) is plotted against normalised depth (depth/indent radius).

which is in moderate agreement with the Hertzian ball on flat contact shear stress field.

The ballistic indent showed a deviation from this distribution, with a second spike in dislocation density at a depth of 0.9 Z. This spike is likely related to the hemispherical band of high dislocation density observed in the map in Fig. 4(c). Similar but significantly smaller versions of this spike in dislocation density can be observed in both the QS and DW line scans. However, the depth of this peak is variable from QS to ballistic rates. All line scans tended to zero at a depth of ≈1.7 Z.

3.3.2. TEM

Electron transparent thin foils were prepared from two locations in the ballistic indent section. Position A corresponds to the central region and position B to the periphery of the indent damage region, as indicated in Fig. 6(a). An SEM cross-sectional view of the specimen in the central region prior to FIB lift-out and final thinning is exemplarily given in Fig. 6(b). Grains are separated by broad boundaries showing darker contrast. The region thinned for TEM analysis is indicated. A TEM bright-field (BF) image of the thin foil of the central region is shown in Fig. 6(c). It includes one broad boundary between two grains filled with amorphous residue, likely from sample preparation. The dark contrast within grains indicates internal stress as well as a network of dislocations. Grain boundaries (GB), pores and cracks are labelled. A detailed view of the dislocation network is given in Fig. 7(a) showing contrast that is caused by extensive distortion from large dislocation densities.

Fig. 6(d) shows a TEM BF image of the thin foil obtained from the periphery of the indent damage region. It shows cracking as well as a series of deformation twins likely introduced by the indentation. In Fig. 7 (b) several parallel aligned deformation twins are shown, terminating at 'Crack (I)'. They measure some tens of nm in width as indicated in Fig. 7(d). A detailed view of dislocation bands crossing 'Crack (II)' are shown in Fig. 7(c), indicating this crack has formed after the dislocations were introduced.

Very high dislocation densities in these regions prevent the full characterisation of defects through resolving dislocations with diffraction-contrast imaging techniques, such as double beam or weak beam. For HCP alumina, (0001) is widely recognised as the main slip plane, but it is likely that pyramidal prism is the dominant glide plane of dislocations, particularly for mechanical deformation under constrained conditions, as noted by Wu et al. [25]. Twins are generally developed along the basal plane with a thickness of ~50 nm along ⟨0001⟩, which is the same as observed in mechanically deformed alumina by grinding operation [25]. There appears to be increased twinning in this sample when compared to alumina after high velocity ballistic testing at speeds of 800–900 m s^{-1} [9], which may further reinforced the conclusion that high strain rate impact tends to reduce twins but boost dislocations.

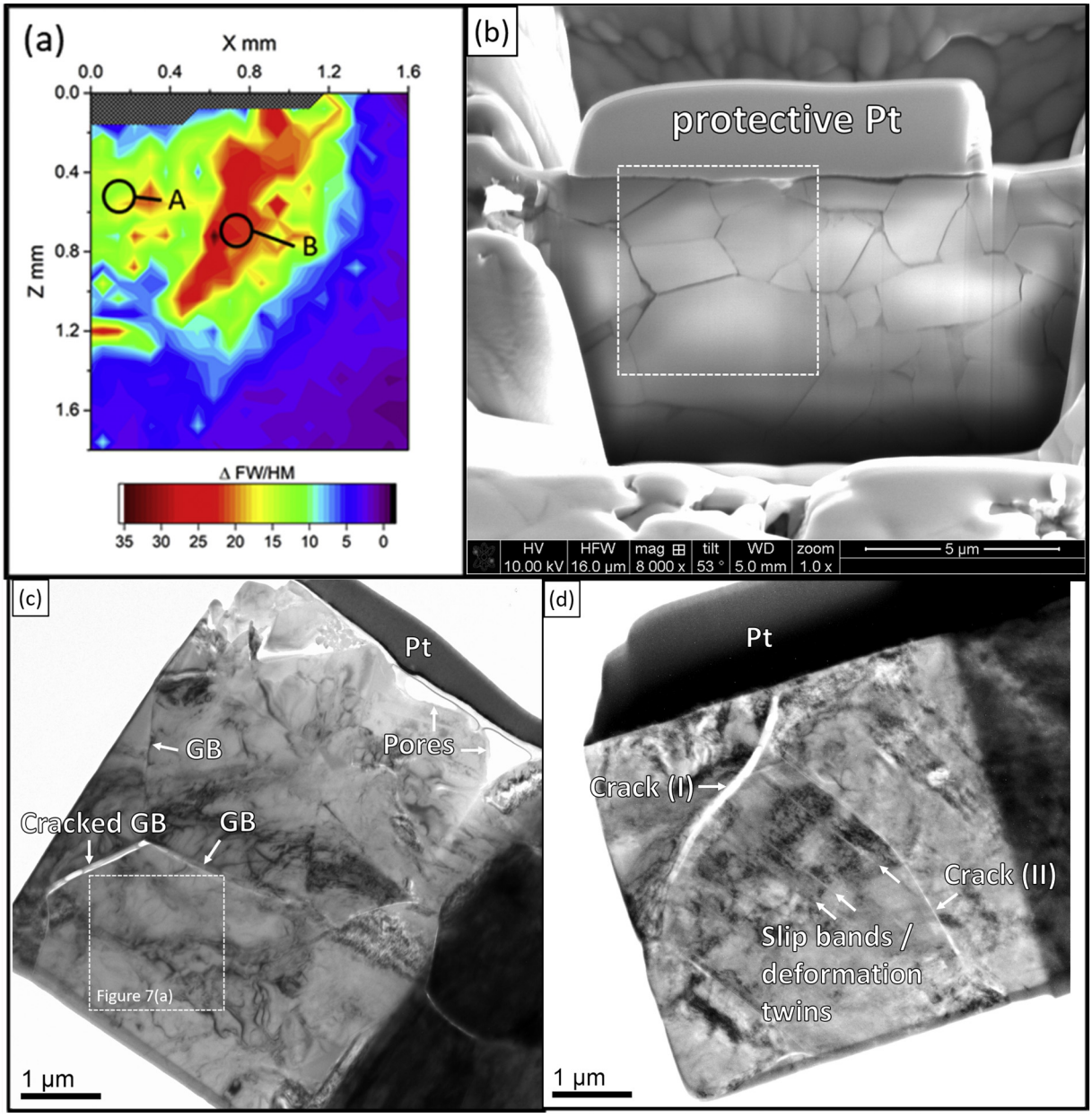

Fig. 6. TEM thin foils of regions of high damage in the ballistic indent. (a) Lift-out locations marked in the fluorescence map, (b) FIB cross-section in central region of the polished indent, (c) TEM bright-field overview of location A thin foil, (d) TEM bright-field overview of location B thin foil.

4. Discussion

4.1. Crack phenomenology

Both surface crack detection and indent sections revealed a clear difference in the form and extent of cracking between quasi-static, dynamic and ballistic indents. The most noticeable difference being the large primary cone crack, generation of spall cracks, and increased lateral cracking in DW indents when compared to quasi-static.

The arching cracks observed outside of the DW indentation were determined to be spall type cracking. Most likely initiating at the cone and propagating laterally, tending to the surface in regions of high tensile stress. This suggests that spall cracking is generated at a similar time to lateral cracking, probably due to rapid indenter unloading or as a result of large reflected tensile stress waves from the rear face of the tile.

Ballistic indents showed significantly greater fragmentation, corresponding to the higher kinetic energy of the projectile and reflected by the larger indent diameter (twice that of DW and QS indents). Sections through these indents exhibited a clear comminuted zone which was bounded by intersecting radial, lateral and cone cracks. The extensive comminuted zone had consumed any evidence of early stage cracking such as ring/cones. The extent of fragmentation and comminution suggests this indent may have surpassed the dwell stage and is in the early stages of projectile penetration.

4.2. Plastic deformation

4.2.1. Under quasi-static impact conditions

Cr^{3+} Fluorescence spectroscopy indicates that ductile deformation (dislocations) is generated in alumina at all tested rates. The extent and distribution of dislocation density being similar in quasi-static and

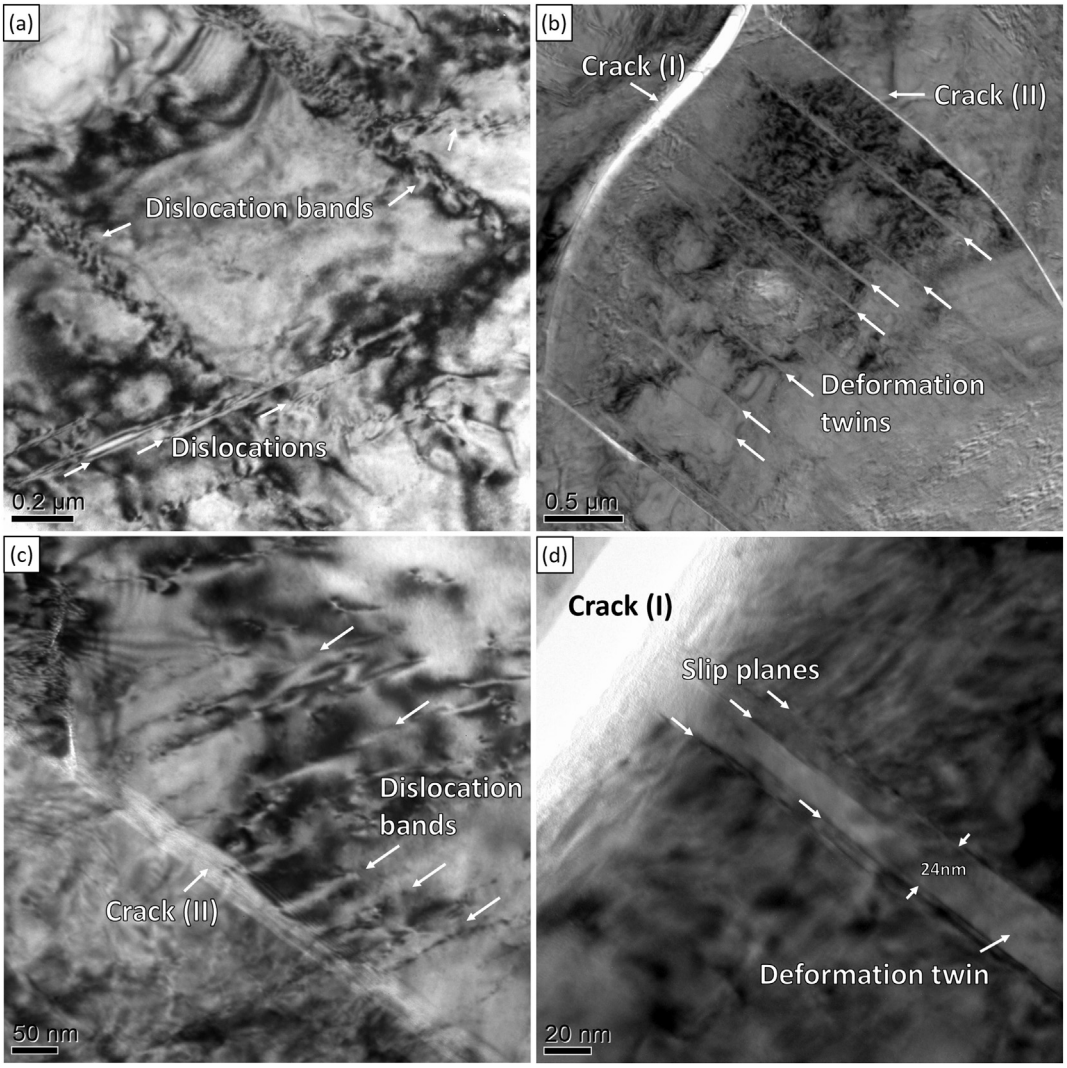

Fig. 7. Correlation plot between ΔFWHM and $\tau - \tau_c$, with a good linear correlation of $R^2 = 0.75$.

drop-weight indentations for comparable indent diameters. Fluorescence spectroscopy maps and lines scans of quasi-static and DW indents show a dislocation density distribution in good agreement with that of the shear stress field predicted by the Hertzian ball indentation model. In this model the shear stress is described by Eq. (4) for depth under the indentation along the loading axis, where depth is described in relation to the coordinate Z, where Z = z/a = depth/indent radius.

$$\frac{\tau_{13}}{\sigma_0} = -(1+\nu)\left[1 - Z\arctan\left(\frac{1}{Z}\right) + \frac{3}{2}\frac{1}{1+Z^2}\right] \quad (4)$$

$$\sigma_0 = \frac{3}{2}P_0 \quad (5)$$

where P_0 is the average indent pressure, σ_0 is the peak indent stress, τ_{13} is shear stress and ν is Poisson's ratio, assigned a typical value of 0.24.

Using the known quasi-static indent load (22 kN) and Eqs. (4) and (5), a shear stress field was modelled for Z under the loading axis (indent radius = 0). This model was compared directly with the high-resolution line scan, as shown in Fig. 8a. It was noted that the ΔFWHM tended to 0 at $Z = 1.69 \pm 0.05$. Using Eqs. (4) and (5) it can be calculated that at $Z = 1.69$, $\tau_{13} = 2.55 \pm 0.10$ GPa. This could be said to be the shear stress threshold (τ_c) for dislocation formation in this grade of alumina.

Table 2 presents a Hertzian quasi-static hardness of this alumina of 12.42 ± 0.24 GPa. Its yield strength should be approximately 1/3 of the hardness: $\sigma_y = 4.14 \pm 0.08$ GPa. Based on von Mises criterion and Tresca criteria, yield strength, σ_y, and critical shear stress, τ_c, have the following relationships, respectively [36].

$$\tau_0 = \frac{1}{\sqrt{3}}\sigma_y$$

$$\tau_0 = \frac{1}{2}\sigma_y \quad (6b)$$

By using Eqs. (6a) and (6b), the corresponding critical shear stress estimated from quasi-static hardness is 2.39 ± 0.05 GPa and 2.07 ± 0.04 GPa, respectively. Based on von Mises criterion, the estimated critical shear stress is very close to the estimated one from the boundary of dislocation map underneath the contact impression. This coincidence demonstrates that the dislocation maps using broadening of Cr^{3+} fluorescence spectrum peak is robust in one side. In addition, a better fitting on van Mises criterion than Tresca may implies that the critical value of stored distortion energy controls the dislocation activity, rather than the maximum shear stress in the material. Such implication is not

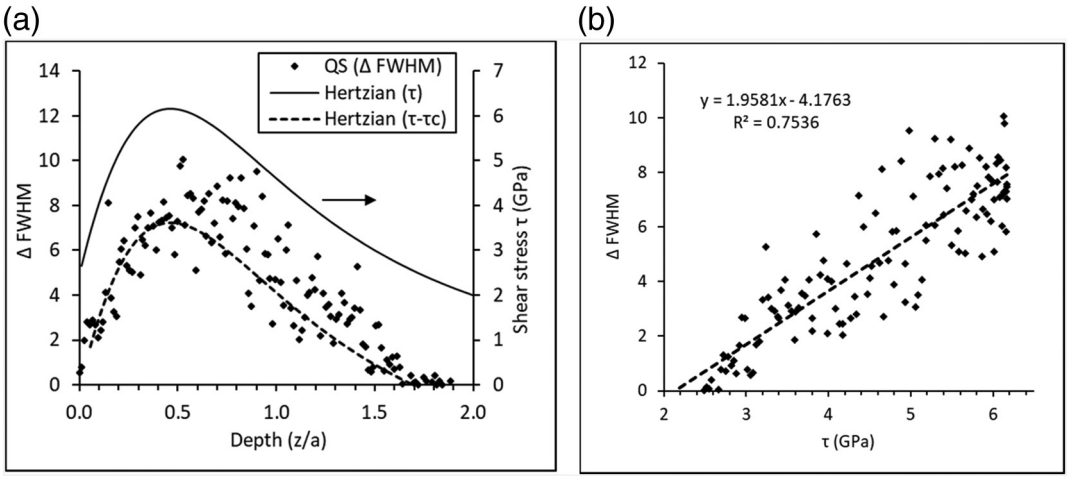

Fig. 8. (a) Primary axis shows a plot of ΔFWHM against depth under the indent. On the secondary axis the Hertzian τ model and Hertzian $\tau - \tau_c$ are plotted against depth under the indent. (b) Correlation plot between ΔFWHM and τ- τ_c, with a good linear correlation of $R^2 = 0.75$.

unreasonable when the dislocation activities happen under constrained conditions by the material surrounding the impact region.

Using this shear stress threshold, a minimum indentation load to generate plastic deformation can be estimated. Indent yield occurs where the maximum shear stress ($\tau_{13}/P_0 = 0.486$) is equal to the shear yield (2.55 ± 0.10 GPa). The minimum mean indent stress (P_0) to induce plastic deformation (yield) is therefore 5.25 ± 0.21 GPa. This is in good agreement with Guiberteau et al. who observed that a mean indent stress of ≈5 GPa is required for the onset of plastic deformation [22]. Variations in this yield stress are most likely due to grain size and glassy phase content [18,22,31].

It should be noted that a compressive yield stress of 5 GPa is significantly larger than the material's specified value of compressive strength of 2.0 GPa. This suggests that yielding *via* ductile deformation occurs only when high confinement is imposed by surrounding material. This fact implies that high constraint is needed for this ceramic to fully fulfil its potential resistance of projectile penetration.

The variation of dislocation density underneath the indent is deemed to be linked to the variation of shear stress level. When Δ FWHM is correlated with the Hertzian shear stress field (τ) a good correlation is observed (Fig. 8b). Hence, the following relations are proposed:

$$\frac{\Delta FWHM}{\phi} = \tau - \tau_c = \Delta\tau \tag{7}$$

where ϕ is a conversion factor determined to be 1.96 cm^{-1}/GPa for this material and τ_c is the critical shear stress previously discussed. A value of critical shear stress can be determined from the intercept of τ where Δ FWHM = 0. This results in a value of τ_c of 2.13 GPa. This value is slightly lower than that previously calculated. Determination of τ_c using this method is highly sensitive to small changes in correlation trend gradient (conversion factor). It should therefore only be used in conjunction with its' respective conversion factor and is most suitable for use in stress extrapolation, not the determination of critical shear stress.

By combining Eqs. (1)–(3) with (6a) and (6b), a relationship between dislocation density and shear stress level can be established above the critical shear stress threshold, as follows.

$$\phi\Delta\tau = K\sqrt{\rho \ln(1/b\sqrt{\rho\pi})} \tag{8}$$

Eqs. (7) and (8) show that, as a first approximation, the square root of dislocation density is proportional to additional shear stress above the critical one for dislocation motion, or the measurement of net broadening of fluorescence peak. For this phenomenological correlation, it is proposed that work hardening is the physical mechanism responsible for the increase of dislocation under a shear stress higher than the critical threshold. During deformation, dislocations pin other dislocations' motion which leads to cold hardening, and the required additional shear stress to overcome obstacles to dislocations is

$$\Delta\tau = \frac{Gb}{L} \tag{9}$$

where L is the projected length between adjacent dislocation obstacles, which is inversely proportional to the square root of dislocation density:

$$L = \frac{1}{\sqrt{\rho}} \tag{10}$$

Combining Eqs. (9) and (10), the additional shear stress and dislocation density have the following relationship:

$$\Delta\tau = Gb\sqrt{\rho} \tag{11}$$

Although Eqs. (8) and (11) are not quite similar, the logarithmic part in Eq. (8) has a minor influence, compared to dislocation density itself. Therefore, the variation in dislocation density under quasi-static loading conditions is likely to result in work hardening inside the indentation.

4.2.2. Global plastic flow under impact

Cr^{3+} − fluorescence spectroscopy mapping of sections through 22 kN QS and DW indents showed a dislocation density distribution in agreement with the Hertzian shear stress field, Fig. 9. The correlation of dislocation density distribution to the Hertzian stress field is only moderate. This is unsurprising as the model is based on the stress distribution for a purely elastic deformation, the plastic deformation and cracking observed is likely to modify the stress field. As indicated by section line scans, the maximum ΔFWHM values for quasi-static and DW indents was at a depth of ≈0.5 Z, which agrees with the Hertzian shear stress model.

In Fig. 4(c), a hemispherical band of high dislocation density is observed. This band primarily contains Δ FWHM values above 20. When the map is adjusted to exclude ΔFWHM values above 20 a second distribution becomes apparent, as shown in Fig. 10. This resembles the Hertzian shear stress field distribution observed in quasi-static and DW indents.

From this it could be suggested that there are at least two stages to the formation of dislocations (plastic deformation). The first is a Hertzian like shear stress field, likely occurring at early stages of contact,

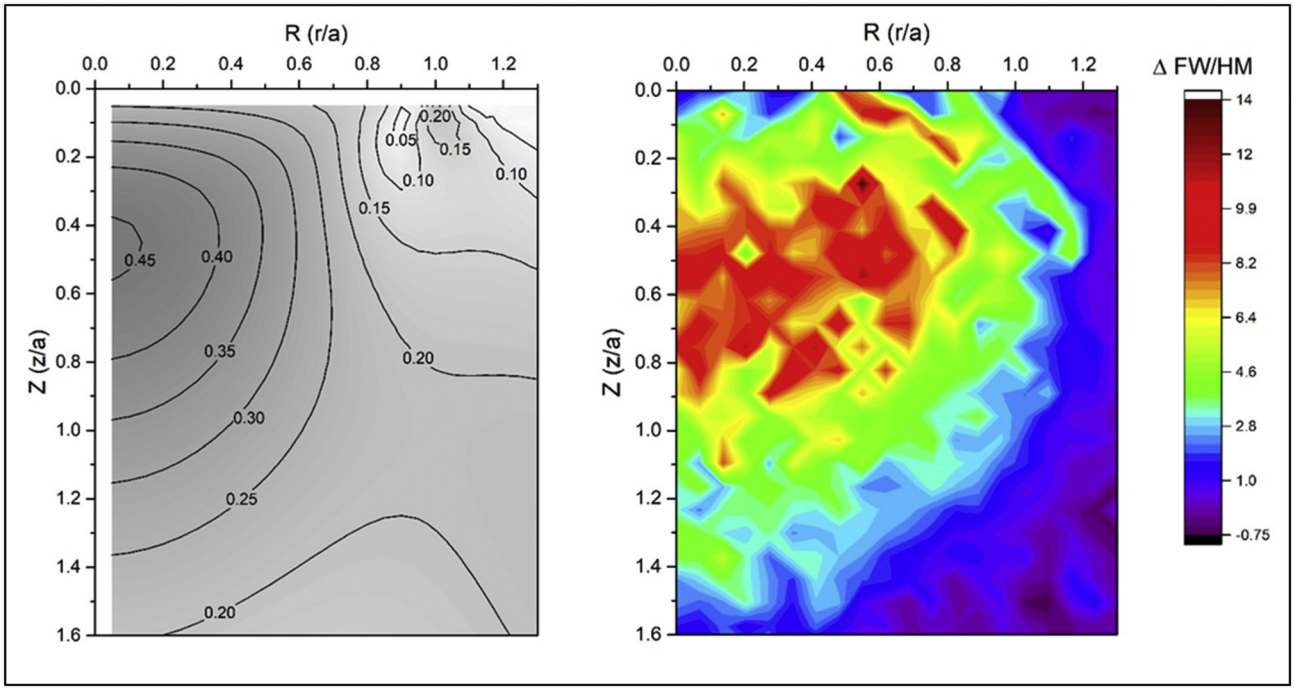

Fig. 9. (left) Hertzian ball on flat shear stress field. (Right) Δ FWHM map of a section through a quasi-static 22 kN indentation.

but under much higher contact pressures than that of quasi-static loading. This extent of Hertzian like deformation is governed by the critical shear stress (shear yield) and work hardening of the material.

The second deformation mechanism is the formation of extremely high dislocation density bands, likely due to material "flow" as large-scale deformation occurs under the impacting projectile.

Using Eq. (7) with $\tau_c = 2.13$ GPa and $\phi = 1.96$ cm^{-1}/GPa, a maximum shear stress contributing to Hertzian like deformation can be established. Taking $\Delta FWHM = 14$ cm^{-1} as the maximum Hertzian contribution we can estimate a shear stress of 9.3 GPa, which, assuming a Hertzian contact stress field (Eqs. 4 and 5) corresponds to a mean dynamic indentation pressure, *i.e.* dynamic hardness under ballistic impact rate, of 19 GPa.

For reference, the mean indentation pressure from the projectile kinetic energy and indentation volume can be estimated using the following [31,37].

$$P_0 = \frac{mu^2}{2\Delta V} \tag{12}$$

where m is the mass of the projectile, u is the velocity of the projectile before impact, a is the contact radius, taken as the radius of the permanent indentation, and ΔV is the change in volume of the indent (0.32 mm^3 measured with confocal microscopy). This results in a mean impact pressure of 40 ± 5 GPa (cumulative error from velocity).

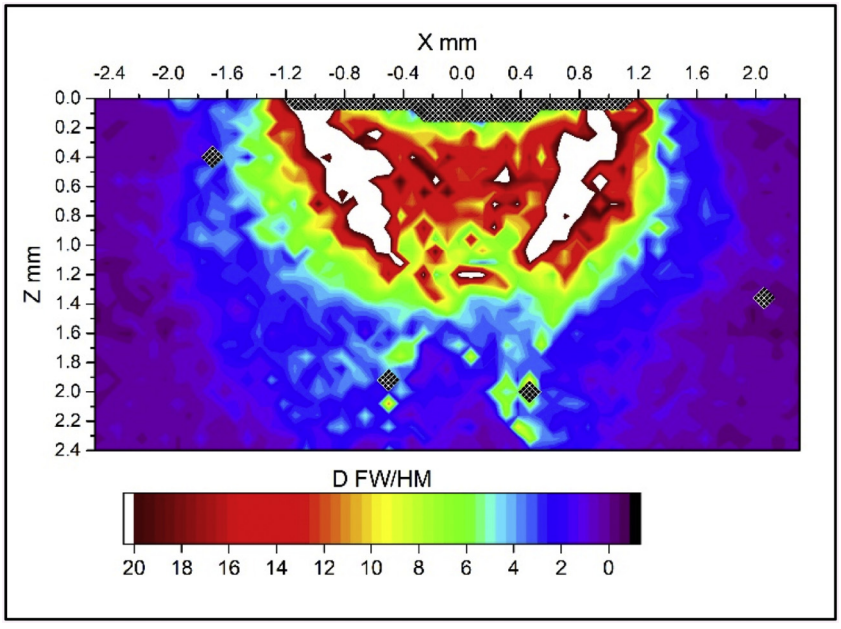

Fig. 10. Cr^{3+} fluorescence map of a section through a ballistic indent with values of >20 Δ FW/HM discounted.

This is slightly in excess of twice the pressure predicted from the Hertzian deformation dislocation density (19 GPa). This suggests that just less than half of the kinetic energy, at 160 m s^{-1}, is dissipated through plastic deformation at the dwell stage of impact. The remaining kinetic energy may be dissipated through fragmentation, fragment flow, and fragment deformation during the penetration of the tile. The fragment deformation is observed as "flow bands" in the ΔFWHM map.

Many have performed quantitative investigations on recovered fragments from ballistic testing, showing that the total fracture surface area during full penetration of alumina is typically 0.05 to 0.4 m^2, including surface area contribution from nanoscale fragments [38,39]. This corresponds to <1% of the kinetic energy dissipated by the alumina [39]. Therefore, the energy for fragmentation is widely regarded to have a minor contribution to ballistic performance. It has been shown that the ballistic performance of pre-fragmented alumina is only reduced by 30 to 40%, with the main energy dissipating mechanisms being fragment erosion, flow and ejection [3] [40].

The high ΔFWHM values (20 to 35 cm^{-1}) observed in the flow bands indicates that high degrees of plastic deformation *via* dislocation generation occur during fragment flow. This in turn suggests that plastic deformation of ceramics continues to play a role in energy dissipation during the penetration stage of impact.

5. Conclusions

Contact impacts under quasi-static, drop-weight and ballistic loading conditions show a similar Hertzian contact characteristic of ductile deformation irrespective of loading rates. Conversely, different loading rates of contact impact leads to variation in cracking/fragmentation patterns. This observation suggests that ductile deformation, through the generation of dislocations, is independent to cracking.

Cross-sectional maps of dislocation density have shown that dislocation distributions inside the ductile deformation regions are equivalent for quasi-static and drop weight indentations, with a maximum of ~1–2 $\times 10^{15}$ m^{-2} at a depth along its median axis of ~0.4–0.7 of the radius of the residual contact impression. This is consistent with the Hertzian shear stress field underneath an elastic flat surface loaded by a rigid ball. Dislocation density is proportional to the level of shear stress, giving a linear correlation between ΔFWHM and shear stress predicted by the Hertzian contact model. A critical shear stress for dislocation generation is hence determined to be 2.55 ± 0.10 GPa for the alumina ceramic tested.

Under ballistic loading conditions, a secondary plastic flow band with a dislocation density up to 10^{16} m^{-2} appeared in addition to the Hertzian dislocation density distribution. This is believed to be dynamic "material flow", occurring at the boundary of the comminuted zone at its incipient stage. The flow bands exhibited a dislocation density 5–10 times higher than the Hertzian deformation. TEM imaging of material from these regions shows a high density of slip bands, twinning and dislocations, supporting the Cr^{3+} fluorescence measurements.

The findings of this study further the understanding of the magnitude and distribution of plastic deformation present during ballistic rate indentations. The determined critical shear stress and relationship between shear stress and dislocation density are valuable factors for the modelling and design of ceramic armour materials.

CRediT authorship contribution statement

Robert G. Crookes: Data curation, Formal analysis, Investigation, Methodology, Validation, Visualization, Writing - original draft.**Benjamin Maerz:**Data curation, Formal analysis, Investigation, Methodology.**Houzheng Wu:**Conceptualization, Funding acquisition, Methodology, Project administration, Supervision, Writing - review & editing.

Declaration of competing interest

The authors declare no conflict of interest related to this paper.

Acknowledgements

We acknowledge and thank Morgan Advanced Materials for supplying the Sintox™ CL alumina tiles tested in this work. The authors acknowledge use of facilities within the Loughborough Materials Characterization Centre.

References

[1] S.M. Walley, Historical review of high strain rate and shock properties of ceramics relevant to their application in Armour, Adv. Appl. Ceram. 109 (2010) 446–466, https://doi.org/10.1179/174367609X422180.
[2] D.A. Shockey, A.H. Marchand, S.R. Skaggs, G.E. Cort, M.W. Burkett, R. Parker, Failure phenomenology of confined ceramic targets and impacting rods, Int. J. Impact Eng. 9 (1990) 263–275, https://doi.org/10.1016/0734-743X(90)90002-D.
[3] A. Krell, E. Strassburger, Order of influences on the ballistic resistance of armor ceramics and single crystals, Mater. Sci. Eng. A 597 (2014) 422–430, https://doi.org/10.1016/j.msea.2013.12.101.
[4] M.L. Wilkins, C. Honodel, D. Sawle, An Approach to the Study of Light Armor, 1967.
[5] M.L. Wilkins, C.F. Cline, C.A. Honodel, Fourth Progress Report of Light Armor Program, 1969https://doi.org/10.2172/4173151.
[6] J. Wade, S. Robertson, Y. Zhu, H. Wu, Plastic deformation of polycrystalline alumina introduced by scaled- down drop-weight impacts, Mater. Lett. 175 (2016) 143–147, https://doi.org/10.1016/j.matlet.2016.04.023.
[7] D. Hallam, A. Heaton, B. James, P. Smith, J. Yeomans, The correlation of indentation behaviour with ballistic performance for spark plasma sintered Armour ceramics, J. Eur. Ceram. Soc. 35 (2015) 2243–2252, https://doi.org/10.1016/j.jeurceramsoc.2014.11.035.
[8] R.M. Anderson, T.A. Adler, J.A. Hawk, Scale of microstructure effects on the impact resistance of Al2O3, Wear. 162–164 (1993) 1073–1080, https://doi.org/10.1016/0043-1648(93)90126-7.
[9] H. Wu, S. Ghosh, C.E. Dancer, R.I. Todd, Ballistic damage in alumina ceramics - learning from fragments, A Collect. Pap. Present. 38th Int. Conf. Adv. Ceram. Compos 2014, pp. 49–62.
[10] A.G. Atkins, D. Tabor, Hardness and deformation properties of solids at very high temperatures, Proc. R. Soc. A Math. Phys. Eng. Sci. 292 (1966) 441–459, https://doi.org/10.1098/rspa.1966.0146.
[11] B.C. Weber, O. Ruff, F. Ebert, E. Cohn, P. Duwez, F. Odell, F.H. Brown, A. Cocco, D. Viechnicki, S. Stubican, D.K. Smith, C.F. Cline, C.F. Grain, R.C. Garvie, E. Klinger, A. Rabenau, Hot hardness of selected borides, oxides, and carbides to 19OO0C, 30 (1967).
[12] A. Krell, O.V. Bakun, High-temperature hardness of Al_2O_3-base ceramics, Acta Metall. 34 (1986) 1315–1319, https://doi.org/10.1016/0001-6160(86)90018-0.
[13] W. Kollenberg, Plastic deformation of Al2O3 single crystals by indentation at temperatures up to 750 °C, J. Mater. Sci. 23 (1988) 3321–3325, https://doi.org/10.1007/BF00551312.
[14] Y.V. Milman, S.I. Chugunova, I.V. Goncharova, T. Chudoba, W. Lojkowski, W. Gooch, Temperature dependence of hardness in silicon-carbide ceramics with different porosity, Int. J. Refract. Met. Hard Mater. 17 (1999) 361–368.
[15] B.J. Hockey, Plastic deformation of aluminum oxide by indentation and abrasion, J. Am. Ceram. Soc. 54 (1971) 223–231, https://doi.org/10.1111/j.1151-2916.1971.tb12277.x.
[16] J.B. Bilde-Sørensen, B.F. Lawlor, T. Geipel, P. Pirouz, A.H. Heuer, K.P.D. Lagerlöf, On basal slip and basal twinning in sapphire (a-Al2O3) - I. basal slip revisited, Acta Mater. 44 (1996) 2145–2152, https://doi.org/10.1016/1359-6454(95)00264-2.
[17] J. Castaing, J. Cadoz, S. Kirby, Deformation of Al2O3 single crystals between 25 °C and 1800 °C: basal and prismatic slip, Le J. Phys. 42 (1981) C3-43–C3-47. http://jphyscol.journaldephysique.org/articles/jphyscol/abs/1981/03/jphyscol198142C304/jphyscol198142C304.html.
[18] S.L. Korinek, J. Castaing, Slip and twinning in polycrystalline alumina (a-Al2O3) deformed under hydrostatic pressure between 600C and 1000C, J. Am. Ceram. Soc. 86 (2003) 566–573, https://doi.org/10.1111/j.1151-2916.1994.tb07006.x.
[19] B.R. Lawn, N.P. Padturet, H. Cait, F. Guiberteaut, Making ceramics "ductile", Science (80-.) 263 (1994) 1114–1116.
[20] B.R. Lawn, Indentation of ceramics with spheres: a century after hertz, J. Am. Ceram. Soc. 81 (2005) 1977–1994, https://doi.org/10.1111/j.1151-2916.1998.tb02580.x.
[21] A.C. Fischer-Cripps, B.R. Lawn, Stress analysis of contact deformation in quasi-plastic ceramics, J. Am. Ceram. Soc. 79 (2005) 2609–2618, https://doi.org/10.1111/j.1151-2916.1996.tb09023.x.
[22] F. Guiberteau, N.P. Padture, B.R. Lawn, Effect of grain size on Hertzian contact damage in alumina, J. Am. Ceram. Soc. 77 (1994) 1825–1831.
[23] B. Lawn, R. Wilshaw, Indentation fracture: principles and applications, J. Mater. Sci. 10 (1975) 1049–1081, https://doi.org/10.1007/BF00823224.
[24] H.Z. Wu, S.G. Roberts, G. Möbus, B.J. Inkson, Subsurface damage analysis by TEM and 3D FIB crack mapping in alumina and alumina/5vol.%SiC nanocomposites, Acta Mater. 51 (2003) 149–163, https://doi.org/10.1016/S1359-6454(02)00387-7.
[25] H. Wu, B.J. Inkson, S.G. Roberts, Subsurface deformation of machined Al2O3 and Al2O3/5vol%SiC nano composite, J. Microsc. 201 (2001) 212–220, https://doi.org/10.1116/1.568601.

[26] F. Longy, J. Cagnoux, Plasticity and microcracking in shock-loaded alumina, J. Am. Ceram. Soc. 72 (1989) 971–979, https://doi.org/10.1111/j.1151-2916.1989.tb06254.x.
[27] J. Lankford, The role of plasticity as a limiting factor in the compressive failure of high strength ceramics, 29 (1998).
[28] N.K. Bourne, J.C.F. Millett, M. Chen, J.W. McCauley, D.P. Dandekar, On the Hugoniot elastic limit in polycrystalline alumina, J. Appl. Phys. 102 (2007) https://doi.org/10.1063/1.2787154.
[29] E.K. Beauchamp, M.J. Carr, R.A. Graham, Plastic deformation in alumina by explosive shock loading, 99 (1985) 696–699.
[30] P. Shukla, R. Crookes, H. Wu, Shock-wave induced compressive stress on alumina ceramics by laser peening, Mater. Des. 167 (2019), 107626. https://doi.org/10.1016/j.matdes.2019.107626.
[31] C.E.J. Dancer, H.M. Curtis, S.M. Bennett, N. Petrinic, R.I. Todd, High strain rate indentation-induced deformation in alumina ceramics measured by Cr 3+ fluorescence mapping, J. Eur. Ceram. Soc. 31 (2011) 2177–2187, https://doi.org/10.1016/j.jeurceramsoc.2011.06.002.
[32] X. Feng, J. Chang, Y. Lu, Experimental research on HEL and failure properties of alumina under impact loading, Def. Technol. 12 (2016) 272–276, https://doi.org/10.1016/j.dt.2016.01.007.
[33] J. Wade, Contact Damage of Ceramics and Ceramic Nanocomposites, Loughborough University, 2017.
[34] H.Z. Wu, S.G. Roberts, B. Derby, Residual stress distributions around indentations and scratches in polycrystalline Al2O3 and Al2O3 / SiC nanocomposites measured using fluorescence probes, Acta Mater. 56 (2008) 140–149, https://doi.org/10.1016/j.actamat.2007.09.014.
[35] J. He, D.R. Clarke, Determination of the Piezospectroscopic coefficients for chromium-doped sapphire, Am. Chem. 78 (1995) 1347–1353.
[36] D. Tabor, Hardness of Metals, Clarendon Press, Oxford, 1951.
[37] Y. Tirupataiah, G. Sundararajan, A dynamic indentation technique for the characterization of the high strain rate plastic flow behaviour of ductile metals and alloys, J. Mech. Phys. Solids. 39 (1991) 243–271, https://doi.org/10.1016/0022-5096(91)90005-9.
[38] E.P. Carton, J. Weerheijm, C. Ditzhuijzen, I. Tuinman, Fragment and particle size distribution of impacted ceramic tiles, 28th Int. Symp. Ballist., Atlanta, USA 2014, pp. 1254–1265.
[39] R.L. Woodward, W.a.A. Gooch, R.G.G. O'Donnell, W.J.J. Perciballi, B.J.J. Baxter, S.D.D. Pattie, A study of fragmentation in the ballistic impact of ceramics, Int. J. Impact Eng. 15 (1994) 605–618, https://doi.org/10.1016/0734-743X(94)90122-2.
[40] I. Horsfall, M.R. Edwards, M.J. Hallas, Ballistic and physical properties of highly fractured alumina, Adv. Appl. Ceram. 109 (2010) 498–503, https://doi.org/10.1179/174367610X12804792635341.